

Total density slope of massive early-type galaxies in Horizon-AGN simulation: impact of AGN feedback and comparison with observations

Sébastien Peirani^{1,2,3,4*}, coauthor^{1,2}, coauthor^{1,3} and ?¹

¹ *Université Côte d’Azur, Observatoire de la Côte d’Azur, CNRS, Laboratoire Lagrange, France*

² *Institut d’Astrophysique de Paris (UMR 7095: CNRS & UPMC), 98 bis Bd Arago, 75014 Paris, France*

³ *Kavli IPMU (WPI), UTIAS, The University of Tokyo, Kashiwa, Chiba 277-8583, Japan*

⁴ *Department of Physics, The University of Tokyo, Tokyo 113-0033, Japan*

⁵ ??????

27 July 2017

ABSTRACT

Using the two large cosmological hydrodynamical simulations, HORIZON-AGN (H_{AGN}) and HORIZON-NOAGN (H_{noAGN} , no AGN feedback), we investigate how a typical sub-grid model for AGN feedback affects the evolution of the total density profiles (dark matter + stars) at the effective radius of massive early-type galaxies ($M_* \geq 10^{11} M_{\odot}$). We have studied the dependencies of the mass weighted density slope γ'_{tot} with the effective radius, the galaxy mass and the host halo mass at $z = 0.25$ and found that the inclusion of AGN feedback always lead to a much better agreement with observational values and trends. Our analysis suggests also that the inclusion of AGN feedback favour a strong correlation between γ'_{tot} and the density slope of the dark matter component while, in the absence of AGN activity, γ'_{tot} is rather strongly correlated with the density slope of the stellar component. **[* Finally, we find that γ'_{tot} derived from our samples of galaxies is slightly increasing from $z = 2$ to $z = 0$, in good agreement with the expected observational trend. However, the derived values are a bit too low when AGN is included because the simulated galaxies tend to be too extended especially for the less massive ones. On the contrary, H_{noAGN} galaxies which are too compact have γ'_{tot} values that are way too high compared to observations.]**

Key words: Galaxies: haloes – Dark matter – Methods: N-body simulations

1 INTRODUCTION

Despite the early discovery of tight scaling relations between the physical properties of the apparently simple “red and dead” population of early-type galaxies (ETGs), the origin and evolution of these relations are still poorly understood (White & Rees 1978; Dressler et al. 1987; Faber et al. 1987; Djorgovski & Davis 1987). These properties concern the stellar mass profile, stellar populations, metallicity, halo mass to stellar mass relation, as well as stellar mass to central supermassive black

hole mass (Magorrian et al. 1998; Ferrarese & Merritt 2000; Häring & Rix 2004; Gültekin et al. 2009). In the standard Λ CDM paradigm, progenitors of massive collapsed structures such as massive ETGs form at high redshift by the accretion of cold filamentary gas (Rees & Ostriker 1977; White & Frenk 1991; Birnboim & Dekel 2003; Kereš et al. 2005; Ocvirk et al. 2008; Dekel et al. 2009; van de Voort et al. 2011) that must be stopped at low redshift by some feedback mechanics coming from the central Active Galactic Nucleus (AGN) (Silk & Rees 1998; King 2003; Wyithe & Loeb 2003).

The emerging picture is that they are formed at a redshift larger than 3 and almost fully assembled by

* E-mail: sebastien.peirani@oca.eu

$z \sim 1$ (e.g. [Renzini 2006](#)). One important conclusion is that their central part must be virialized with a self-similar structure as early as $z \sim 1$ ([Sheth et al. 2003](#)) irrespective of the continuous accretion of dark and luminous matter within the Λ CDM hierarchical merging process. This ETG property may be explained if internal regions (within ~ 2 effective radii) behave like a dynamical attractor featuring an invariant phase space density in spite of their accretion history ([Loeb & Peebles 2003](#)). The dark matter and stellar components seem to work together in building a “universal” nearly isothermal total density profile, even though neither of these components is well approximated by an isothermal profile.

Great observational progress has been achieved in the past few years with the systematic study of early-type galaxies acting as strong gravitational lenses. For these systems, strong lensing provides an absolute measurement of the total mass with a few percent accuracy at a fiducial radius (the Einstein radius). Used in combination with traditional diagnostics such as stellar velocity dispersion ([Miralda-Escude 1995](#); [Natarajan & Kneib 1996](#); [Treu & Koopmans 2002](#); [Sand et al. 2002](#); [Newman et al. 2009](#)), and stellar mass maps from multicolor imaging and/or spectroscopy, one can break many of the degeneracies inherent to each method alone, including the mass-anisotropy degeneracy, bulge-halo degeneracy, and the stellar mass/initial mass function (IMF) degeneracy (e.g. [Koopmans & Treu 2003](#); [Treu & Koopmans 2004](#); [Treu et al. 2010](#); [Auger et al. 2010](#); [Dutton et al. 2013](#)). Additional information can be gathered with the addition of weak-lensing ([Gavazzi et al. 2007](#); [Jiang & Kochanek 2007](#); [Lagattuta et al. 2010](#)), although at the moment this is not possible for individual galaxies. [**✳ Another way to break the degeneracy in the analysis of strong lens systems is to use quasar microlensing which directly measures the stellar mass function at the image position (e.g. [Gavazzi et al. 2014a](#); [Schechter et al. 2014](#); [Jiménez-Vicente et al. 2015](#)).**]

The big sample assembled by the SLACS teams have shown that lensing galaxies are indistinguishable from non-lensing early-type galaxies with similar velocity dispersions in terms of their internal properties and environment ([Bolton et al. 2006](#); [Koopmans et al. 2006](#); [Treu et al. 2006](#); [Gavazzi et al. 2007](#); [Bolton et al. 2008](#); [Treu et al. 2009](#); [Koopmans et al. 2009](#); [Auger et al. 2009, 2010](#); [Barnabè et al. 2011](#); [Czoske et al. 2012](#); [Shu et al. 2015](#)). Additional samples of higher redshift lenses with measured velocity dispersion have then been built ([Tu et al. 2009](#); [Gavazzi et al. 2014b](#); [Ruff et al. 2011a](#); [Sonnenfeld et al. 2013a](#); [Gavazzi et al. 2012](#); [Sonnenfeld et al. 2013b, 2015](#), Strong Lensing Legacy Survey) ([Brownstein et al. 2012](#); [Bolton et al. 2012](#); [Shu et al. 2016](#), BOSS Emission-line Lens Survey) and allowed to investigate the time dependence of the slope of the inner total mass density profile near the effective radius (see also [Tortora et al. 2014](#); [Dye et al. 2014](#); [Posacki et al. 2015](#); [Smith et al. 2015](#)). At fixed mass, the slope correlates with the projected stellar mass density seems to decrease with redshift while remaining

close to isothermal ($\gamma' \equiv -d \log \rho / d \log r \simeq 2$, with a noticeably small $\sim 6\%$ intrinsic scatter). Similar conclusions can be drawn from spatially resolved stellar kinematics of ETGs (see e.g. [Cappellari 2016](#), for a review). In addition, the combination of strong lensing and stellar kinematics at groups and clusters scales can also provide us with sizable statistical samples ([Newman et al. 2013, 2015](#)) for extending our understanding of galaxy formation towards the high mass end.

In parallel to these observational efforts, several attempts were made to understand the origin and the tightness of this relation, either with semi-analytical models or idealized simulations ([Nipoti et al. 2009](#); [Lackner & Ostriker 2010](#); [Nipoti et al. 2012](#); [Lackner et al. 2012](#); [Hirschmann et al. 2012](#); [Johansson et al. 2012](#); [Remus et al. 2013](#); [Dutton & Treu 2014](#); [Sonnenfeld et al. 2014](#); [Shankar et al. 2017](#)). The complex coupling of scales (from dark matter halos and beyond to star formation and AGN activity) involved for the understanding of dynamical interplay between baryons and Dark Matter halos requires very demanding numerical hydrodynamical simulations. An important step forward was made possible by zoomed hydrodynamical simulations around massive galaxies that contain realistic accretion scenarios and sufficient resolution to recover with good fidelity the internal structure of massive ETGs ([Dubois et al. 2013](#)). In particular, a detailed census on the role the feedback from the central AGN was made showing that the quenching of star formation by the central engine is not only important to reproduce stellar to halo mass relations and colors but also to reproduce the size and the dynamical structure (pressure support instead of rotation). The small statistics permitted with these zooms has recently been alleviated by an hydrodynamical simulation with RAMSES ([Teyssier 2002](#)) of larger cosmological volumes containing $\sim 10^5$ objects with similar resolution. This was one of the purposes of the HORIZON-AGN simulation ([Dubois et al. 2014](#); [Welker et al. 2015](#); [Dubois et al. 2016](#)), who confirmed with greater statistics some of the results of [Dubois et al. \(2013\)](#).

Recently a comparison of the internal structure of massive ETGs in the Illustris Simulation which is quite comparable to HORIZON-AGN ([Xu et al. 2017](#)) showed a reasonable agreement with observations, although the size of galaxies seems to be slightly overshoot. This confirms the interest of performing detailed comparisons between simulations and observations with different simulation codes and solvers in order to study degeneracies between subgrid physical recipes and solver specificities that could match observations for very different physical reasons. Hence, since we already studied in detail the role of AGN feedback on the evolution of internal dark matter and stellar density profiles from our set of HORIZON-AGN simulations with RAMSES ([Peirani et al. 2016](#)), we will now attempt to compare our results with the SLACS+SL2S lensing observational constraints on the internal structure of massive galaxies coming from strong lensing + dynamics, the main focus being the total mass density profile within the effective radius.

The paper is organized as follows. Section 2 briefly describes the numerical modelling used in this work (simulations and post-processing) while Section 3 presents our main results relative to the evolution of the total density profiles in massive ETGs. We finally conclude in Section 4.

2 NUMERICAL MODELLING

2.1 Horizon-AGN and Horizon-noAGN simulations

In this paper, we analyse and compare two large cosmological hydrodynamical simulations, HORIZON-AGN (H_{AGN}) and HORIZON-NOAGN (H_{noAGN}). HORIZON-AGN is already described in Dubois et al. (2014), so we only summarise here its main features. We adopt a standard Λ CDM cosmology with total matter density $\Omega_m = 0.272$, dark energy density $\Omega_\Lambda = 0.728$, amplitude of the matter power spectrum $\sigma_8 = 0.81$, baryon density $\Omega_b = 0.045$, Hubble constant $H_0 = 70.4 \text{ km s}^{-1} \text{ Mpc}^{-1}$, and $n_s = 0.967$ compatible with the WMAP-7. The size of the simulated volume is $L_{\text{box}} = 100 h^{-1} \text{ Mpc}$ on a side, and it contains 1024^3 dark matter (DM) particles, which results in a DM mass resolution of $M_{\text{DM, res}} = 8.27 \times 10^7 M_\odot$. The simulation is run with the RAMSES code (Teyssier 2002), and the initially uniform grid is adaptively refined down to $\Delta x = 1$ proper kpc at all times. Refinement is triggered in a quasi-Lagrangian manner: if the number of DM particles becomes greater than 8, or the total baryonic mass reaches 8 times the initial DM mass resolution in a cell.

Gas can radiatively cool down to 10^4 K through H and He collisions with a contribution from metals using rates tabulated by Sutherland & Dopita (1993). Heating from a uniform UV background takes place after redshift $z_{\text{reion}} = 10$ following Haardt Haardt & Madau (1996). The star formation process is modelled using a Schmidt law: $\dot{\rho}_* = \epsilon_* \rho / t_{\text{ff}}$ for gas number density above $n_0 = 0.1 \text{ H cm}^{-3}$, where $\dot{\rho}_*$ is the star formation rate density, ϵ_* = 0.02 the constant star formation efficiency, and t_{ff} the local free-fall time of the gas. The stellar mass resolution is $M_{*, \text{res}} = 2 \times 10^6 M_\odot$. Feedback from stellar winds, supernovae type Ia and type II are also taken into account for mass, energy and metal release (Kimm et al. 2012).

Black hole (BH) formation is also included, and BHs accrete gas at a Bondi-capped-at-Eddington rate and coalesce when they form a tight enough binary. They also release energy in a quasar (heating) or radio (kinetic jet) mode when the accretion rate is above (below) one per cent of Eddington, with efficiencies tuned to match the BH-galaxy scaling relations (see Dubois et al. (2012) for detail). The presence of both quasar and radio modes is supported by recent observations. In particular, using MaNGA data (Bundy et al. 2015), Cheung et al. (2016) report the presence of bi-symmetric emission features in the centre of quiescent galaxies of mass around $2 \times 10^{10} M_\odot$ from which they infer the presence of centrally driven winds. On top of

the fact that such ‘‘red geysers’’ galaxies seem to be very common at this mass scale (Bundy et al., in prep), the energy released by their SMBHs is capable of driving the observed winds and displays a mechanical content sufficient to suppress star formation. It is therefore very likely that such kinetic winds (radio mode) play a crucial role in galaxy formation and should be taken into account in numerical models (see for instance, Weinberger et al. (2016)).

2.2 Galaxy catalogues

Galaxies are identified using the ADAPTAHOP (sub)halo finder (Aubert et al. 2004). We use here the most bound particle as the definition of their centre and only galaxies with more than 50 star particles are part of the final catalogue.

We have also computed the merger trees of the stellar component for each simulation using TREEMAKER (Tweed et al. 2009). We have considered 52 outputs between $z \sim 5.8$ and $z = 0$ at different times equally spaced in time (250 Myr). For instance, in the HORIZON-AGN run, we have identified at $z = 0$ 250,000 haloes and subhaloes with a mass greater than $10^{10} M_\odot$ and 125,000 galaxies with a mass greater than $10^8 M_\odot$.

For each H_{AGN} or H_{noAGN} galaxy, we first find the galaxy spin by measuring its angular momentum vector from stars. This spin vector defines the orientation of the z-axis cylindrical coordinate system within which we compute the radial, tangential and vertical velocity components of each stellar particle. The rotational velocity V of the galaxy is the average of the tangential velocity component. The velocity dispersion is obtained from the dispersion of the radial σ_r , the tangential σ_θ and the vertical velocity σ_z components around their averaged values, i.e. $\sigma^2 = (\sigma_r^2 + \sigma_\theta^2 + \sigma_z^2)/3$. In our analysis, we will select in general H_{AGN} and H_{noAGN} galaxies with $V/\sigma < 1$. **[* Note that past numerical works suggest that the presence of AGN feedback can transform rotationally-supported discs ($V/\sigma > 1$) into dispersion-dominated ellipsoids ($V/\sigma < 1$) (Dubois et al. 2013, 2016). (OTHER REFS?). Therefore, when using our matching algorithm, H_{AGN} galaxies with $V/\sigma < 1$ might be associated to H_{noAGN} galaxies satisfying $V/\sigma > 1$. In the following, we will study the evolution of massive H_{AGN} and H_{noAGN} ETGs galaxies with a mass greater than $10^{11} M_\odot$ and $V/\sigma < 1$.]**

[* Finally, dark matter haloes are also identified with ADAPTAHOP. Their centre coincides with the centre of their hosted galaxies.]

2.3 Matching dark matter haloes and galaxies

Since we start from the same initial conditions, each dark matter particle possesses an identity which is identical in any of the 2 simulations. Thus, if 75% or more of the particles of any given halo in the HORIZON-AGN run also belong to a halo identified in the HORIZON-NOAGN run, we initially assume that these haloes are twins. However, if the mass ratio of the

matching pair is greater than 10 (or lower than 0.1), we exclude it from our comparison sample. This last step is rendered necessary because sub-structures can get their particles stripped by the host halo at different times and with different intensities in the three simulations. As a result, a subhalo could become twinned with a much more massive host halo if its equivalent subhalo in the other simulation has already been destroyed (or has become too small to be detected). In general, we are able to match more than 85% of dark matter objects at any redshift by applying these two criteria.

We cannot implement the same procedure for galaxies since a given stellar particle is not necessarily created at the exact same moment in the very same galaxy in HORIZON-AGN and HORIZON-NOAGN. Moreover, the total number of stellar particles will also differ as it depends on the impact AGN feedback has on the star formation process. Therefore, instead of relying upon a common identity of the stellar particles they are composed of to directly match objects between runs, we first couple each galaxy to a host dark matter halo in their parent simulation. We determine these galaxy-halo pairs by picking the most massive galaxy whose centre is located within a sphere of radius equal to 5% of the virial radius of its host halo. Galaxy twins between runs are then determined through the matching of their host halo as previously described.

To illustrate the typical efficiency of such a procedure, at $z = 0$, we are able to match about 80% of H_{AGN} galaxies with a mass greater $10^{11}M_{\odot}$ to H_{noAGN} counterparts. We have checked that relaxing the quite stringent criteria adopted in this work (slightly) improves the matching fraction, but since it also increases the number of false matches and does not alter any of our conclusions, we prefer to restrict ourselves to the more conservative sample defined in this section.

3 THE TOTAL DENSITY SLOPES AT THE EFFECTIVE RADIUS

3.1 Definitions

In the present study, we focus on the *mass-weighted density slope within r_1 and r_2* introduced by Dutton & Treu (2014):

$$\gamma' = \frac{1}{M(r_2) - M(r_1)} \int_{r_1}^{r_2} \gamma(x) 4\pi x^2 \rho(x) dx \quad (1)$$

where $\gamma \equiv -d \log \rho / d \log r$ is the local logarithmic slope of the density profile ρ and M the local mass. Using a discrete representation of each density profile, $\gamma(r)$ and $M(r)$ can be estimated within each radial bin.

For each studied galaxy, we have considered a random orientation in space and then derive the effective radius R_e at which half of the projected stellar mass is enclosed. Finally, in order to estimate γ' at R_e , we consider the interval $[r_1 - r_2] = [R_e/2 - R_e]$. **[* Note that the simulation grid size has a value of 1 kpc where dark matter or galaxy density profiles might not fully converge. if one follows Power et al. (2003), a lower limit value**

of 5 kpc is more recommended for the studied halo/galaxy mass range, though their analysis concerns pure dark matter simulations only. In general, the effective radius of H_{AGN} galaxies is always larger than 5 kpc. However, This is not the case for H_{noAGN} galaxies and therefore, in certain cases, we will remove galaxies with a too low effective radius (i.e. $R_e \ll 5$ kpc).]

In the following, we will refer γ'_{dm} , γ'_* and γ'_{tot} the mass-weighted density slope derived from the dark matter component, the stellar component and the dark matter + stellar components.

3.2 Dependencies of γ'_{tot} with R_e , M_{halo} and M_*

Fig. 1 shows the variations of the effective radius R_e with respect to the stellar mass M_* for H_{AGN} and H_{noAGN} galaxies with a mass greater than $10^{11}M_{\odot}$ and $V/\sigma < 1$ at $z = 0.25$. **[* We chose this latter value because the observational data we want to compare with, in particular SLACS [* ref?], SL2S [* ref?] and Newman et al. (2013, 2015), are centred around this value.]** In the absence of AGN feedback, the simulated galaxies are generally clearly too compact with an effective radius too small, compared to observational data. **[* Note that for H_{noAGN} galaxies with $\log(M_*) < 11.5$ however, the theoretical predictions seems to agree well with observations. This might be due to the fact that as the effective radius get closer to the resolution limit, their estimation might be overestimated.]** On the contrary, AGN feedback tends to form more extended galaxies as already noted by Dubois et al. (2013). In this case, high-mass ellipticals in HORIZON-AGN are in good agreement with the observations while low-mass ellipticals seem to be not compact enough. **[* YOHAN, any comments???. Also, it is worth mentioning that lensing probability p is a steep function of the velocity dispersion of galaxies (i.e. $p \approx \sigma^4$). Then, for a given stellar mass, more compact galaxies will be selected by using survey which can partly explain the discrepancies between theoretical predictions and observations here. In the following, in order to take into account this selection effect, estimations of the mean value of γ'_{tot} are weighted by σ^4 .]**

Fig. 2 shows the variations of the mass-weighted total density slope γ'_{tot} with respect to the effective radius R_e at $z = 0.25$ for H_{AGN} and H_{noAGN} galaxies with a mass greater than $10^{11}M_{\odot}$ and $V/\sigma < 1$. When comparing our results to observations, we get a much better agreement when AGN feedback is taken into account. Indeed, we found that γ'_{tot} derived from HORIZON-AGN simulation is decreasing with R_e which is consistent with the observational trend. On the contrary, an opposite evolution is obtained when AGN is not included suggesting that more extended galaxies (or more massive galaxies) tend to have higher γ'_{tot} values. Moreover, for $R_e \geq 10$ kpc, the predicted γ'_{tot} values derived from the HORIZON-AGN simulation are in good agreement with those of observations. In particular, we get density slopes close to 2 for the less massive galaxies

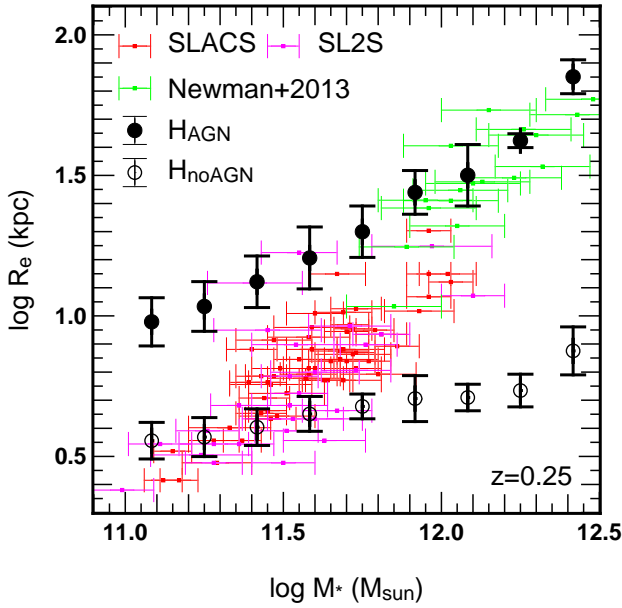


Figure 1. The variations of the effective radius R_e with respect to the stellar mass M_* . Results are derived from H_{AGN} (black points) and H_{noAGN} (white points) galaxies satisfying $V/\sigma < 1$ and $\log(M_*) > 11$ at $z = 0.25$. We also plot observational data from the SLACS, SL2S and Newman et al. (2013) which cover the redshift range of [0.063 - 0.884] but centred around $z \sim 0.25$. Error bars indicate the dispersions.

of our sample which are values expected from the observations. We cannot match the observations for $R_e < 10$ kpc since H_{AGN} low mass elliptical galaxies are too extended as shown in Fig. 1.

From the same samples of galaxies at $z = 0.25$ (i.e. $M_* \geq 10^{11} M_\odot$ and $V/\sigma < 1$), we also take an interest in studying the variations of γ'_{tot} with respect to either the dark matter haloes masses M_{halo} or stellar masses M_* . Those variations are displayed in Fig. 3 and 4 respectively. We find similar trends than those obtained in Fig. 2. First, the presence or not of AGN feedback leads to opposite evolutions. When AGN feedback is included, γ'_{tot} is decreasing with M_{halo} or M_* . In other words, more massive objects tends to have more flat total density profiles at the scale of the effective radius. A similar conclusion was obtained in Peirani et al. (2016), when studying the inner DM and stellar profiles ($r \leq 5$ kpc) which is mainly explained by the fact that AGN feedback has a more important impact in the most massive objects. Moreover, values of γ'_{tot} are in nice agreement with observational ones. On the contrary, in the absence of AGN feedback, γ'_{tot} values are much too high especially for massive objects. Note that we didn't use our matching scheme here when selecting the H_{noAGN} galaxies in order to consistently compare with the observational mass range. However, we have checked that the matching scheme would select H_{noAGN} galaxies with higher masses and higher effective radius but will not really change the evolutions of γ'_{tot} previously derived. [★ It is also encouraging to notice that our simulated values for H_{AGN} haloes presented in Fig. 3 are in nice agreement with those

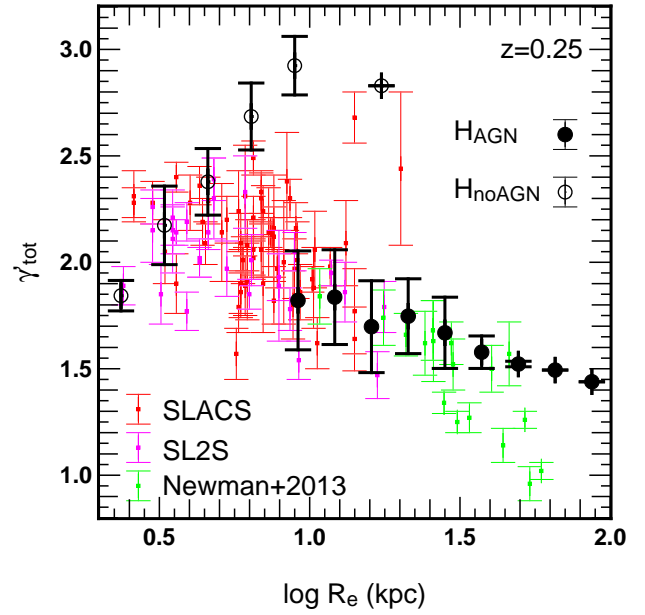


Figure 2. The variations of the mass-weighted total density slopes γ'_{tot} with respect to the effective radius R_e . Results are derived from H_{AGN} (black points) and H_{noAGN} (white points) galaxies with $V/\sigma < 1$ and a mass of $\log(M_*) > 11$ at $z = 0.25$. We also plot observational data from SLACS (red colors), SL2S (pink colors) and Newman et al. (2013) (green colors). Error bars indicate the dispersions. AGN feedback is again required to improve the agreement between theoretical predictions and observational trends.

of Schaller et al. (2015) using the Eagle simulation (Schaye et al. 2015).]

In view of all of these results, AGN feedback seems to be required to explain the observational trends.

3.3 Dependencies of γ'_{tot} with f_{dm}

[★ Another interesting correlation is expected between the mass-weighted total density slope γ'_{tot} and the central dark matter fraction, $f_{\text{dm}}(< r)$, ratio of the dark matter mass and total (dark matter+stellar) mass. In Fig. 5, we then first study the variations of γ'_{tot} with respect to the dark matter fraction within one effective radius $f_{\text{dm}}(< R_e)$ at $z = 0.25$. Comparison with observational expectations indicates that although values derived from H_{AGN} galaxies seems to be in good agreement with the observational trend namely γ'_{tot} is decreasing with f_{dm} , predicted dark matter fraction are generally too high ($f_{\text{dm}} > 0.5$) in the considered galaxy mass range. Values derived from H_{noAGN} galaxies are this time much lower ($f_{\text{dm}} > 0.5$) but with γ'_{tot} too high. In Fig. 6, we plot $f_{\text{dm}}(< r)$ as a function of the scale normalized to the effective radius at $z = 0.25$ and for two separated samples namely galaxy satisfying $11.3 < \log(M_*) < 11.5$ and $6 < R_e/\text{kpc} < 10$, and galaxies satisfying $12 < \log(M_*)$. When comparing to observational predictions from Sonnenfeld et al.

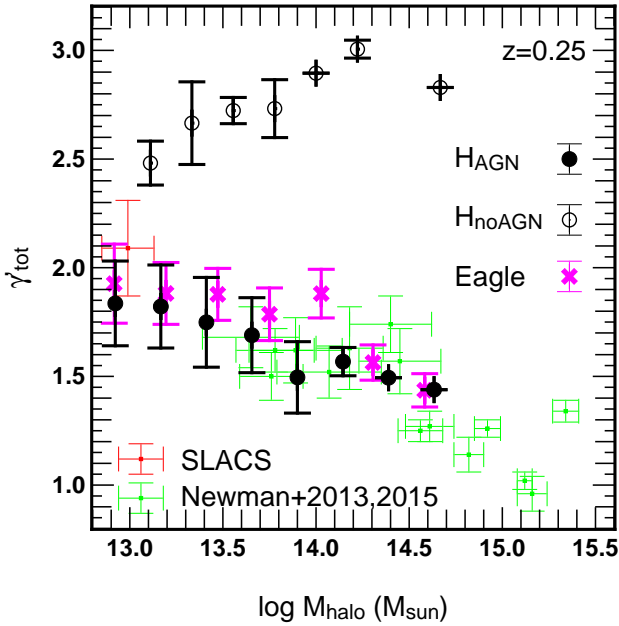


Figure 3. The variations of the mass-weighted total density slopes γ'_{tot} with respect to the dark matter halo masses M_{halo} . Results are derived from H_{AGN} (black points) and H_{noAGN} (white points) galaxies with $V/\sigma < 1$ and a mass of $\log(M_*) > 11$ at $z = 0.25$. We also plot observational data from SLACS (red colors) and Newman et al. (2013, 2015) (green colors) [**as well as predictions from the Eagle simulation.**] Error bars indicate the dispersions. When AGN feedback is included, theoretical predictions are in nice agreement with observations. On the contrary, in the absence of AGN feedback, derived γ'_{tot} values are totally inconsistent with observational expectations.

(2015) and Newman et al. (2013), it seems that our predicted $f_{dm}(< r)$ is overestimated for the less massive galaxies while the agreement with more massive ones is much better. This plots confirms that for the less massive galaxies, theoretical f_{dm} within one effective radius is clearly too high compare to Sonnenfeld et al. finding. Finally, in Fig. 7, we plot the average $f_{dm}(< r)$ derived from our samples of H_{AGN} galaxies at four different redshifts. One can notice that $f_{dm}(< r)$ is regularly increasing from $z = 2$ to $z = 0$, especially at small scales ($r < R_e$). OTHER comparison? Masamune'ones?]

3.4 Dependencies of γ'_{tot} with γ'_{dm} and γ'_*

In this section, we investigate the variations of γ'_{tot} with either the stellar slope γ'_* or the dark matter slope γ'_{dm} for galaxies with a mass greater than $10^{11} M_{\odot}$ and $V/\sigma < 1$ at $z = 0.25$. Results from HORIZON-AGN and HORIZON-NOAGN simulations are presented in Fig. 8. First, when AGN feedback is included, one can notice that γ'_{tot} and γ'_{dm} are strongly correlated. Regarding the dependency of γ'_{tot} and γ'_* , the dispersion is higher and the correlation is less clear but the important point here is that AGN feedback tends to limit the total slope to values close to 2 for the less massive galaxies while it

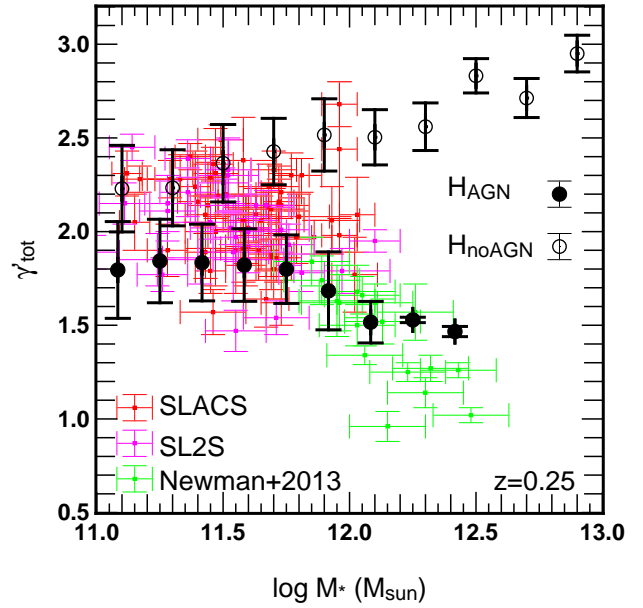


Figure 4. The variations of the mass-weighted total density slopes γ'_{tot} with respect to the stellar masses M_* at $z = 0.25$. Results are derived from H_{AGN} (black points) and H_{noAGN} (white points) galaxies with $V/\sigma < 1$ and a mass of $\log(M_*) > 11$. We also plot observational data from SLACS (red colors), SL2S (pink colors) and Newman et al (2013) (green colors). Error bars indicate the dispersions. AGN feedback permits to get a pretty good agreement with observations.

duces γ'_{tot} in the more massive ones, which is consistent with the observations. On the contrary, in the absence of AGN feedback, we found again the opposite trends: γ'_{tot} and γ'_* are this time strongly correlated and due to stronger adiabatic contraction, γ'_{dm} reach values too high in more massive objects (see Peirani et al. (2016)).

Another way to look into those variations and potential strong correlations between the three different density slopes is to consider the 2d-plots of Fig. 9 showing the variations of γ'_* and γ'_{dm} with a color code representing the values of γ'_{tot} for galaxies with a mass greater than $10^{11} M_{\odot}$ and $V/\sigma < 1$ at $z = 0$. Note that this time we use the matching algorithm to select the H_{noAGN} galaxies which has the advantage, beside comparing the same objects between the simulations, to consider a higher number of H_{noAGN} galaxies. Indeed, most of the massive H_{noAGN} galaxies are disk-dominated and do no then satisfied $V/\sigma < 1$ (see Dubois et al. (2016)). However, we have checked that no significant difference are obtained if H_{noAGN} galaxies were selected using the same mass and V/σ criteria. Thus, the plots presented in Fig. 9 give the possible pairs $(\gamma'_{dm}, \gamma'_*)$ for a given value of γ'_{tot} . We also see the linear correlations between γ'_{tot} and γ'_{dm} and between γ'_{tot} and γ'_* when AGN is included or not respectively.

The strong correlations seen between γ'_{tot} and γ'_{dm} or γ'_{tot} and γ'_* when AGN is included or not respectively can be easily understood when studying the density profile of the different components of a single object shown in Fig. 10. When AGN is included, galaxies are more

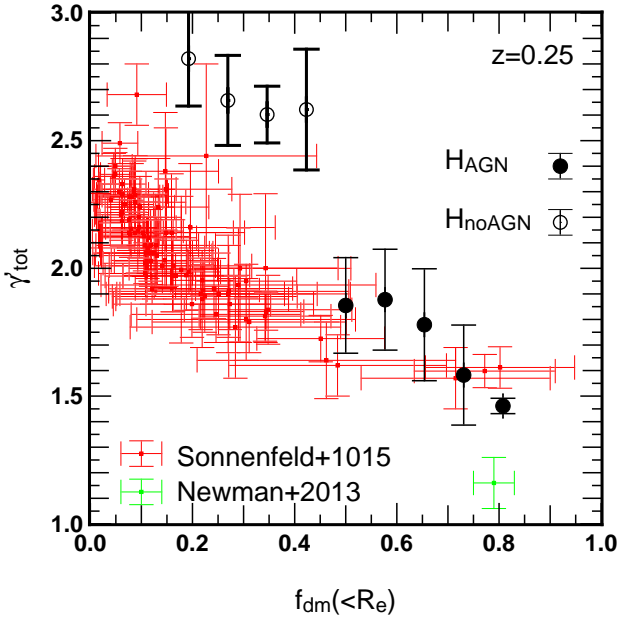


Figure 5. [★ The variations of the mass-weighted total density slopes γ'_{tot} with respect to the dark matter fraction within one effective radius $f_{dm}(<R_e)$. Results are derived from H_{AGN} (black points) and H_{noAGN} (white points) galaxies with $V/\sigma < 1$ and a mass of $M_* > 10^{11}M_\odot$ at $z = 0.25$. We also show derived observational values from Sonnenfeld et al. (2015) (red points) using ... and Newman et al. (2013) (green point). While values from H_{AGN} are in good agreement with the observational trend, it seems however that the dark matter fraction are generally too high ($f_{dm} > 0.5$) in the considered galaxy mass range. Error bars indicate the dispersions.]

extended and therefore have higher effective radius in general. Consequently, the dark matter is the dominant component at the effective radius scale. On the contrary, galaxies are proved to be very compact in the absence of AGN activity and have therefore a smaller effective radius. In this case, the stellar component is the dominant component at the effective radius scale as it is clearly shown in Fig. 10.

3.5 Evolutions of γ'_{tot} between $0 \leq z \leq 2$

One of the main objectives of this paper is to make theoretical predictions of the time evolution of γ'_{tot} of massive ETGs. Fig. 11 presents the time evolution of γ'_{dm} , γ'_* and γ'_{tot} for H_{AGN} galaxies with a mass greater than $10^{11}M_\odot$ and $V/\sigma < 1$ in the considered redshift interval. We also impose $R_e > 5$ kpc in order to be not too close to the lower resolution limit. We also derived evolutions from associated H_{noAGN} galaxies. Note that we analyse here the evolution from $z = 2$ since our resolution does not enable us to properly estimate the different density slopes at higher z as typical effective radius of galaxies at higher redshift becomes too small. When considering H_{AGN} galaxies, we see a slight increase with time of the dark matter and total density slopes while the stellar density slope is nearly constant and close to 2.3

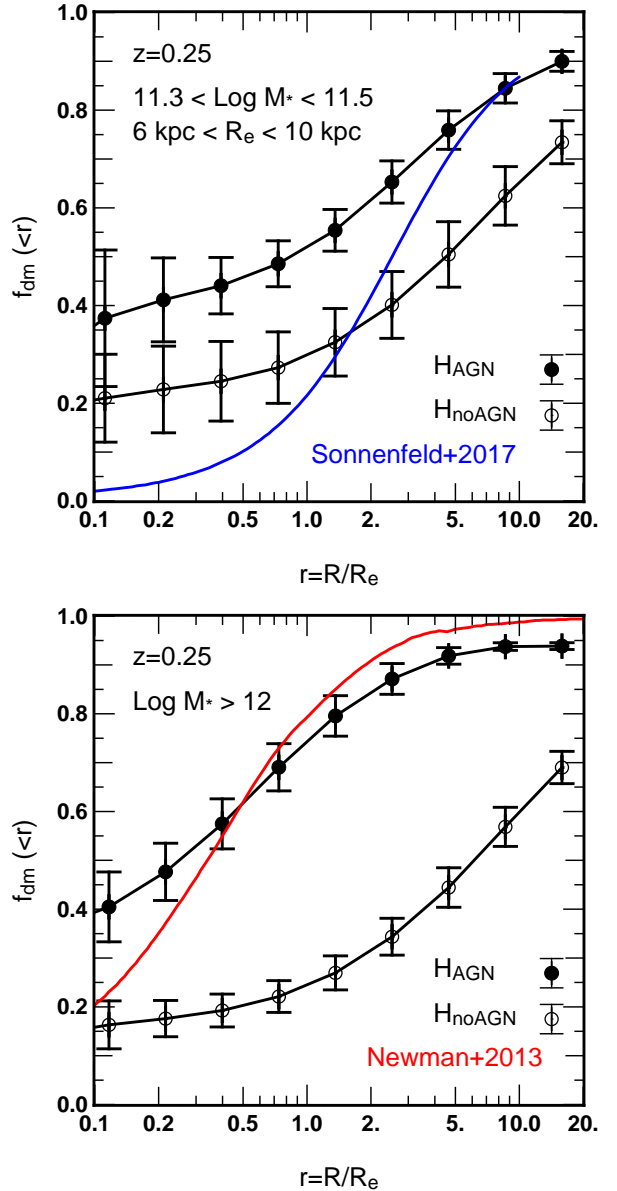


Figure 6. [★ Dark matter fraction $f_{dm}(<r)$ as a function of the scale normalized to the effective radius. Results from H_{AGN} (black points) and H_{noAGN} (white points) galaxies with a mass greater with $V/\sigma < 1$ at $z = 0.25$. We consider two separated samples to compare to available observations: galaxies that satisfy $11.3 < \log(M_*) < 11.5$ and $6 < R_e/\text{kpc} < 10$ (upper panel) and galaxies with a mass greater than $M_* > 10^{12}M_\odot$ (lower panel). Again, we compare to observational data from Sonnenfeld et al. (in prep) and Newman et al. (2013). Error bars indicate the dispersions.]

in the considered redshift interval. This means that the dark matter and total density profiles estimated at the effective radius tend to become slightly more steep at low redshifts while the stellar one does not vary significantly. The situation is slightly different for matching H_{noAGN} galaxies. In this case, contrary to γ'_{dm} which is increasing, γ'_* and therefore γ'_{tot} seem to be almost constant after $z = 1$. Note that an additional level of

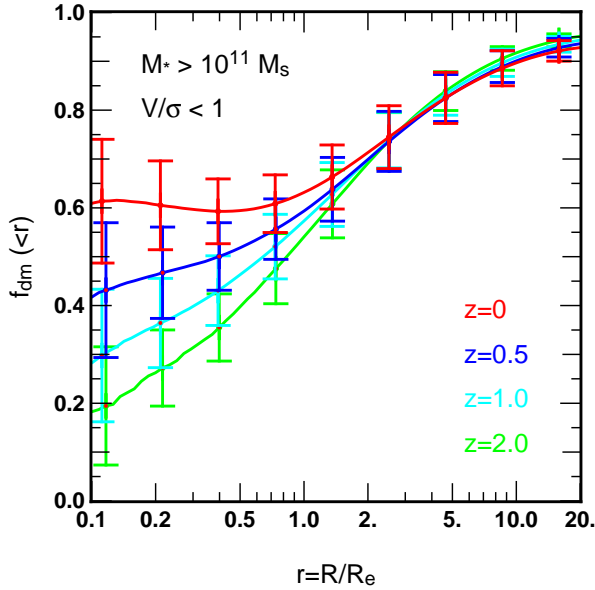


Figure 7. [★ Dark matter fraction $f_{dm}(< r)$ as a function of the scale normalized to the effective radius. Results from H_{AGN} galaxies with a mass greater than $10^{11}M_{\odot}$ and $V/\sigma < 1$ are displayed for four different redshifts: 2.0 (green line), 1.0 (cyan line), 0.5 (blue line) and 0 (red line). Error bars indicate the dispersions.]

refinement occurs at $z \sim 0.5$ and induces a bump in their evolutions. But despite of this, it appears clearly that when AGN is not taken into account, the density slopes of each component is always higher than H_{AGN} counterparts.

Finally, we directly compare the evolutions of γ'_{tot} to observations in Fig. 12. We consider here galaxies satisfying $M_* \geq 10^{11}M_{\odot}$, $V/\sigma < 1$ and $R_e > 5$ kpc in the redshift range of $0 \leq z \leq 2$. In the absence of AGN feedback, the derived γ'_{tot} values are too high compared to observations, as expected. When AGN feedback is included, the derived γ'_{tot} values are this time a bit too low. The observational data suggest that γ'_{tot} is also slightly increasing in the interval $0 \leq z \leq 0.8$ though there is a big dispersion in the data. Our theoretical prediction from $HORIZON-AGN$ exhibits then a much better agreement but it is not yet fully satisfactory. The discrepancies with observations could be explained by the fact that the H_{AGN} galaxies are too extended as shown in Fig. 1. Having galaxies slightly more compact, especially for the low mass ellipticals, will tend to increase values of γ'_{tot} and therefore improve greatly the matching with observations.

[★ The slight increase of γ'_{tot} in the considered redshift interval seems to be due to the increase of the density slope of the DM component as suggested by Figs 11, 8 and 9. And as shown in Peirani et al. (2016), this latter evolution is due to the fact as the AGN become less efficient at low z , the inner DM density profiles tend to become more and more steep. Also, it is worth mentioning that Dubois et al. (2016)

have shown that for a given stellar mass, R_e is generally increasing with time. Therefore, from Fig. 2, one would rather expect that this size-redshift evolution would lead to lower γ'_{tot} values at low redshift, which is not the case. Therefore, the slope evolution derived from $HORIZON-AGN$ in Fig. 12 cannot be totally interpreted as a consequence of the size-redshift evolution of galaxies. (NOT SURE THIS IS SO SIMPLE...)]

4 DISCUSSION AND CONCLUSIONS

By comparing results from two state-of-the-art hydrodynamical cosmological simulations whose only difference is the presence/absence of AGN feedback we have explored the impact of AGN feedback on the evolution of the total density profiles of massive early-type galaxies. We mainly focused on galaxies with a mass greater than $10^{11}M_{\odot}$ and satisfying $V/\sigma < 1$. Our findings can be summarized as follows:

- In the absence of AGN feedback, the simulated galaxies are clearly too compact with an effective radius too small, compared to observational data. On the contrary, AGN feedback tends to form more extended galaxies as already noted by Dubois et al. (2013, 2016). In this case, high-mass ellipticals in $HORIZON-AGN$ seems to be in good agreement with the observations while low-mass ellipticals are not compact enough.
- When studying the variations of γ'_{tot} with the effective radius, the galaxy mass and the host halo mass at $z = 0.25$, we found that the inclusion of AGN feedback is required to get a much better agreement with observational values and trends.
- γ'_{tot} is strongly correlated with γ'_{dm} when AGN feedback is included. On the contrary, γ'_{tot} is strongly correlated with γ'_* in the absence of AGN feedback.
- γ'_{tot} is slightly increasing between $0 \leq z \leq 2$. This is due to the fact that when AGN is included, the evolution of γ'_{tot} is correlated with the evolution of γ'_{dm} . In Peirani et al. (2016), we indeed found that the dark matter density slope is increasing at low redshift because the AGN activity is reduced.

One interesting prediction of the present analysis is the evolution of γ'_{tot} over the cosmic time. Because of our limited resolution (1 physical kpc), we could only considered the interval $0 \leq z \leq 2$. When AGN is included, we found that γ'_{tot} is slightly increasing with time. Compared to observational values, this trend is quite consistent though simulated values are a bit too low. This could be explained by the fact that the less massive H_{AGN} galaxies of our samples seem to be too extended. It is worth mentioning that observations from strong lensing by Ruff et al. (2011b) and Bolton et al. (2012) suggest that the total density profile of massive galaxies has become slightly steeper over cosmic time, in agreement with our finding. However, using well resolved hydrodynamical simulations, Remus et al. (2017); Xu et al. (2017) found the opposite trend i.e., γ'_{tot} is decreasing after $z = 2$. Probably, the key point here is the behaviour and values of γ'_{tot} before $z = 2$. If important sources of feedback (e.g. AGN quasar mode)

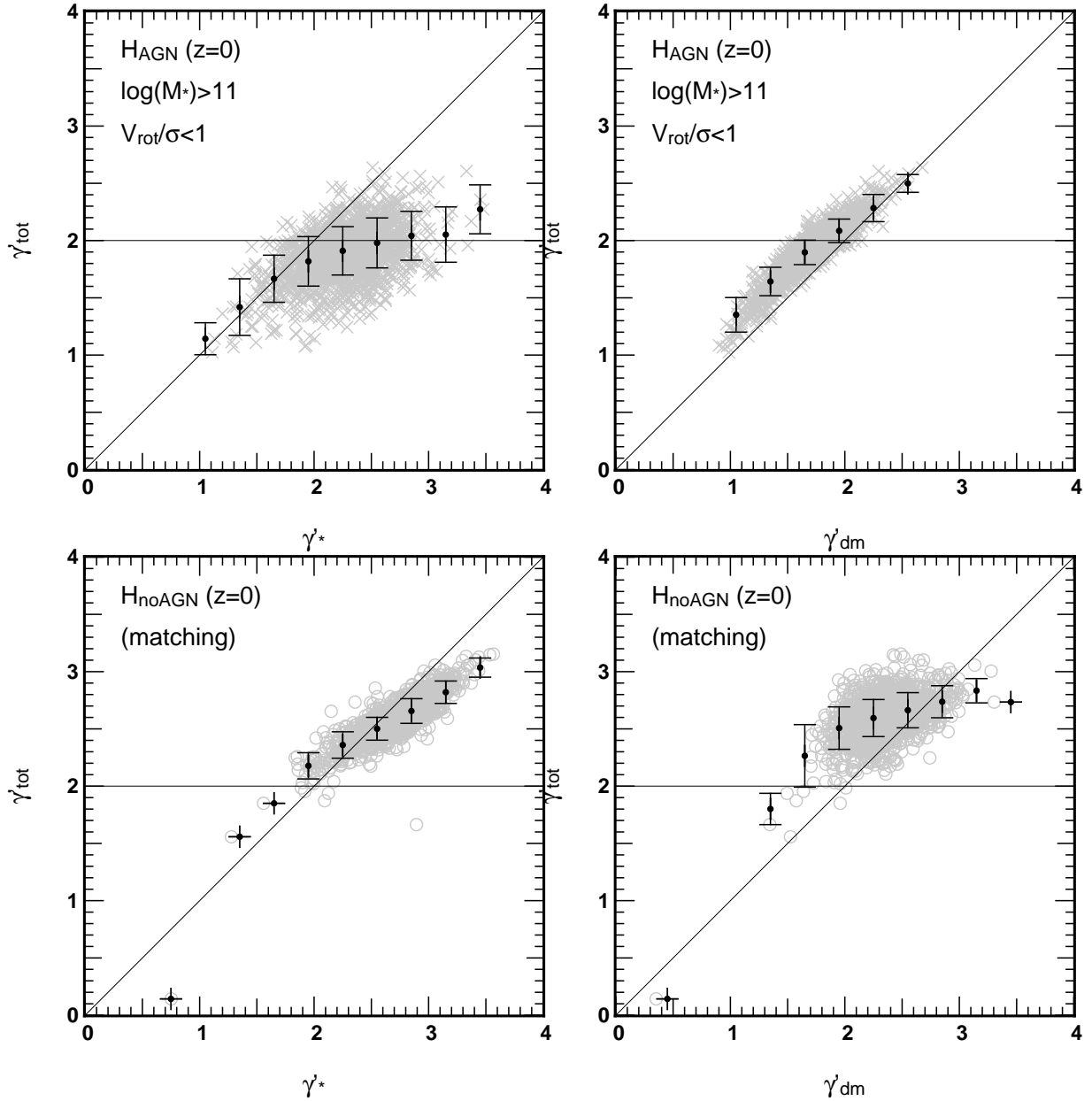


Figure 8. First line: the variations of the mass-weighted total density slope γ'_{tot} with respect to the mass-weighted stellar density slope γ'_* (first column) or the mass-weighted dark matter density slope γ'_{DM} (second column) for H_{AGN} galaxies with a mass greater than $10^{11} M_{\odot}$ and $V/\sigma < 1$ at $z=0.25$. Results from the matching H_{noAGN} galaxies are displayed in the second line. The horizontal solid line represents $\gamma'_{\text{tot}} = -2$ generally obtained in the observation while the diagonal one is $y = x$.

can flatten the dark matter and stellar components at high redshift, then it would be difficult to sustain such flat profiles at lower redshift if feedback become less efficient as advocated by Peirani et al. (2016). On the contrary, if those different components are already steep at $z = 2$, then mechanisms such as (dry) major mergers ([\star Sonnenfeld, Nipoti & Treu 2014]) or efficient feedback could more easily flatten them at low z . The observational data of the SLACS, SL2S and BELLS seems to suggest that γ'_{tot} is slightly increasing but future detailed observational data, especially before $z = 2$, will definitely help to constraint the different scenarios and theoretical models.

Acknowledgements

We warmly thanks M. Schaller for providing relevant Eagle simulation data. S. P. acknowledges support from the Japan Society for the Promotion of Science (JSPS long-term invitation fellowship). This work was granted access to the HPC resources of CINES under the allocations 2013047012, 2014047012 and 2015047012 made by GENCI and has made use of the Horizon cluster hosted by the Institut d’Astrophysique de Paris on which the simulation was post-processed. This work was carried out within the framework of the Horizon project (<http://www.projet-horizon.fr>) and is partially supported by the grants ANR-13-BS05-0005 of the French

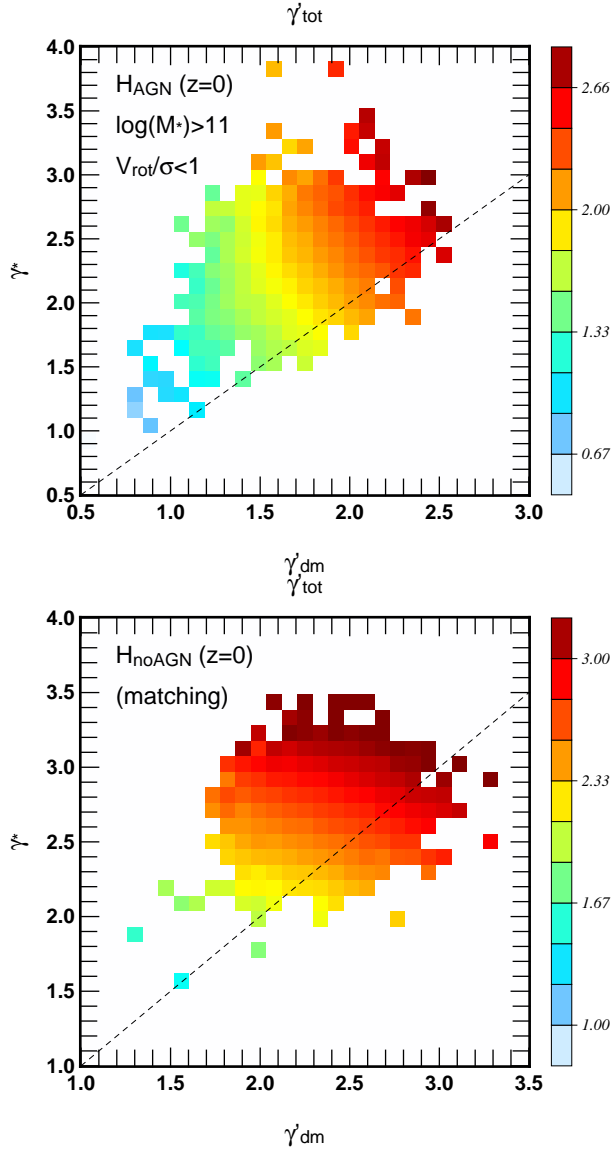


Figure 9. The variations of the mass-weighted stellar density slope γ'_* with respect to the mass-weighted dark matter density slope γ'_{dm} for H_{AGN} galaxies with a mass greater than $10^{11} M_{\odot}$ and $V/\sigma < 1$ at $z=0$ (left panel) and matching H_{noAGN} galaxies (right panel). The color code represents values of the mass-weighted total density slope γ'_{tot} . The dashed line indicates $y = x$.

Agence Nationale de la Recherche. The research of J. D. is supported by Adrian Beecroft and STFC.

REFERENCES

- Aubert, D., Pichon, C., & Colombi, S. 2004, MNRAS, 352, 376
 Auger, M. W., Treu, T., Bolton, A. S., et al. 2009, ApJ, 705, 1099
 Auger, M. W., Treu, T., Bolton, A. S., et al. 2010, ApJ, 724, 511
 Barnabè, M., Czoske, O., Koopmans, L. V. E., Treu, T., & Bolton, A. S. 2011, MNRAS, 415, 2215
 Binboim, Y. & Dekel, A. 2003, MNRAS, 345, 349

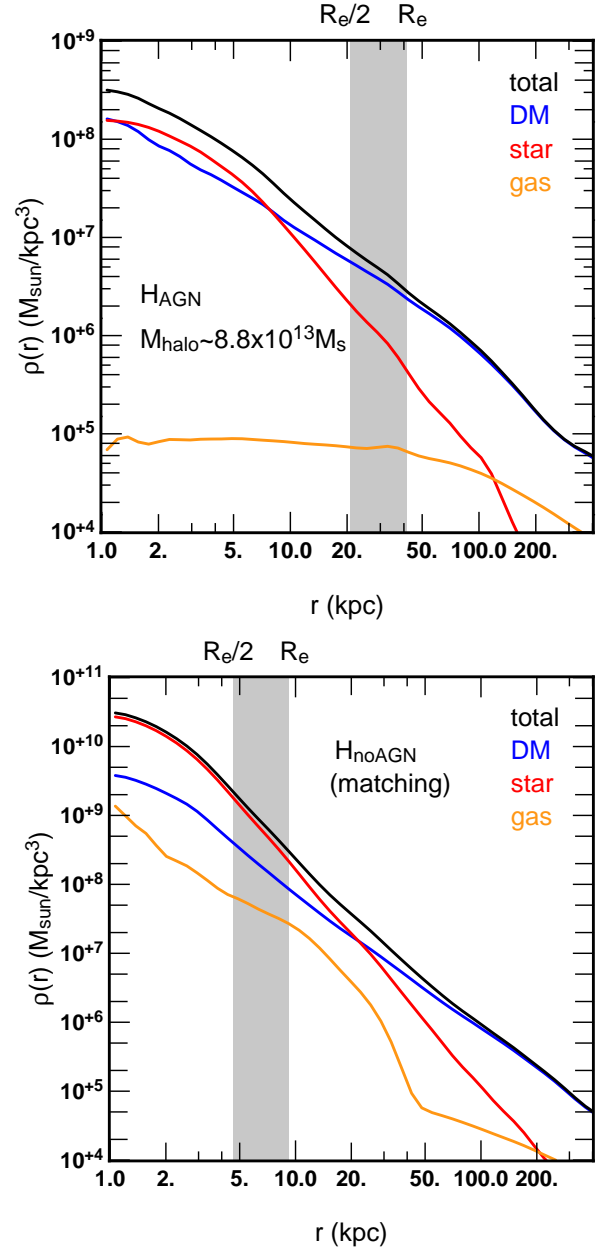


Figure 10. The total density profile (black lines) of the same massive dark matter halo extracted from the HORIZON-AGN (upper) and HORIZON-AGN (lower) simulations at $z = 0$. The dark matter, stellar and gas components are also shown in blue, red and orange colors respectively. The grey shade areas indicate the range of $[R_e/2 - R_e]$ i.e. where we compute γ'_{tot} , γ'_* and γ'_{dm} .

- Bolton, A. S., Brownstein, J. R., Kochanek, C. S., et al. 2012, ArXiv e-prints
 Bolton, A. S., Burles, S., Koopmans, L. V. E., et al. 2008, ApJ, 682, 964
 Bolton, A. S., Burles, S., Koopmans, L. V. E., Treu, T., & Moustakas, L. A. 2006, ApJ, 638, 703
 Brownstein, J. R., Bolton, A. S., Schlegel, D. J., et al. 2012, ApJ, 744, 41
 Bundy, K., Bershady, M. A., Law, D. R., et al. 2015, ApJ, 798, 7

- Cappellari, M. 2016, *ARA&A*, 54, 597
- Cheung, E., Bundy, K., Cappellari, M., et al. 2016, *Nature*, 533, 504
- Czoske, O., Barnabè, M., Koopmans, L. V. E., Treu, T., & Bolton, A. S. 2012, *MNRAS*, 419, 656
- Dekel, A., Birnboim, Y., Engel, G., et al. 2009, *Nature*, 457, 451
- Djorgovski, S. & Davis, M. 1987, *ApJ*, 313, 59
- Dressler, A., Lynden-Bell, D., Burstein, D., et al. 1987, *ApJ*, 313, 42
- Dubois, Y., Devriendt, J., Slyz, A., & Teyssier, R. 2012, *MNRAS*, 420, 2662
- Dubois, Y., Gavazzi, R., Peirani, S., & Silk, J. 2013, *MNRAS*, 433, 3297
- Dubois, Y., Peirani, S., Pichon, C., et al. 2016, *MNRAS*, 463, 3948
- Dubois, Y., Pichon, C., Welker, C., et al. 2014, *MNRAS*, 444, 1453
- Dutton, A. A., Macciò, A. V., Mendel, J. T., & Simard, L. 2013, *MNRAS*
- Dutton, A. A. & Treu, T. 2014, *MNRAS*, 438, 3594
- Dye, S., Negrello, M., Hopwood, R., et al. 2014, *MNRAS*, 440, 2013
- Faber, S. M., Dressler, A., Davies, R. L., Burstein, D., & Lynden-Bell, D. 1987, in *Nearly Normal Galaxies. From the Planck Time to the Present*, ed. S. M. Faber, 175–183
- Ferrarese, L. & Merritt, D. 2000, *ApJ*, 539, L9
- Gavazzi, R., Marshall, P. J., Treu, T., & Sonnenfeld, A. 2014a, *ApJ*, 785, 144
- Gavazzi, R., Marshall, P. J., Treu, T., & Sonnenfeld, A. 2014b, *ApJ*, 785, 144
- Gavazzi, R., Treu, T., Marshall, P. J., Brault, F., & Ruff, A. 2012, *ApJ*, 761, 170
- Gavazzi, R., Treu, T., Rhodes, J. D., et al. 2007, *ApJ*, 667, 176
- Gültekin, K., Richstone, D. O., Gebhardt, K., et al. 2009, *ApJ*, 698, 198
- Haardt, F. & Madau, P. 1996, *ApJ*, 461, 20
- Häring, N. & Rix, H.-W. 2004, *ApJ*, 604, L89
- Hirschmann, M., Naab, T., Somerville, R. S., Burkert, A., & Oser, L. 2012, *MNRAS*, 419, 3200
- Jiang, G. & Kochanek, C. S. 2007, *ApJ*, 671, 1568
- Jiménez-Vicente, J., Mediavilla, E., Kochanek, C. S., & Muñoz, J. A. 2015, *ApJ*, 799, 149
- Johansson, P. H., Naab, T., & Ostriker, J. P. 2012, *ApJ*, 754, 115
- Kereš, D., Katz, N., Weinberg, D. H., & Davé, R. 2005, *MNRAS*, 363, 2
- Kimm, T., Kaviraj, S., Devriendt, J. E. G., et al. 2012, *MNRAS*, 425, L96
- King, A. 2003, *ApJ*, 596, L27
- Koopmans, L. V. E., Bolton, A., Treu, T., et al. 2009, *ApJ*, 703, L51
- Koopmans, L. V. E. & Treu, T. 2003, *ApJ*, 583, 606
- Koopmans, L. V. E., Treu, T., Bolton, A. S., Burles, S., & Moustakas, L. A. 2006, *ApJ*, 649, 599
- Lackner, C. N., Cen, R., Ostriker, J. P., & Joung, M. R. 2012, *MNRAS*, 425, 641
- Lackner, C. N. & Ostriker, J. P. 2010, *ApJ*, 712, 88
- Lagattuta, D. J., Fassnacht, C. D., Auger, M. W., et al. 2010, *ApJ*, 716, 1579
- Loeb, A. & Peebles, P. J. E. 2003, *ApJ*, 589, 29
- Magorrian, J., Tremaine, S., Richstone, D., et al. 1998, *AJ*, 115, 2285
- Miralda-Escude, J. 1995, *ApJ*, 438, 514
- Natarajan, P. & Kneib, J.-P. 1996, *MNRAS*, 283, 1031
- Newman, A. B., Ellis, R. S., & Treu, T. 2015, *ApJ*, 814, 26
- Newman, A. B., Treu, T., Ellis, R. S., & Sand, D. J. 2013, *ApJ*, 765, 25
- Newman, A. B., Treu, T., Ellis, R. S., et al. 2009, *ApJ*, 706, 1078
- Nipoti, C., Treu, T., Auger, M. W., & Bolton, A. S. 2009, *ApJ*, 706, L86
- Nipoti, C., Treu, T., Leauthaud, A., et al. 2012, *MNRAS*, 422, 1714
- Ocvirk, P., Pichon, C., & Teyssier, R. 2008, *MNRAS*, 390, 1326
- Peirani, S., Dubois, Y., Volonteri, M., et al. 2016, *ArXiv e-prints*
- Posacki, S., Cappellari, M., Treu, T., Pellegrini, S., & Ciotti, L. 2015, *MNRAS*, 446, 493
- Power, C., Navarro, J. F., Jenkins, A., et al. 2003, *MNRAS*, 338, 14
- Rees, M. J. & Ostriker, J. P. 1977, *MNRAS*, 179, 541
- Remus, R.-S., Burkert, A., Dolag, K., et al. 2013, *ApJ*, 766, 71
- Remus, R.-S., Dolag, K., Naab, T., et al. 2017, *MNRAS*, 464, 3742
- Renzini, A. 2006, *ARA&A*, 44, 141
- Ruff, A. J., Gavazzi, R., Marshall, P. J., et al. 2011a, *ApJ*, 727, 96
- Ruff, A. J., Gavazzi, R., Marshall, P. J., et al. 2011b, *ApJ*, 727, 96
- Sand, D. J., Treu, T., & Ellis, R. S. 2002, *ApJ*, 574, L129
- Schaller, M., Frenk, C. S., Bower, R. G., et al. 2015, *MNRAS*, 452, 343
- Schaye, J., Crain, R. A., Bower, R. G., et al. 2015, *MNRAS*, 446, 521
- Schechter, P. L., Pooley, D., Blackburne, J. A., & Wambsgans, J. 2014, *ApJ*, 793, 96
- Shankar, F., Sonnenfeld, A., Mamon, G. A., et al. 2017, *ApJ*, 840, 34
- Sheth, R. K., Bernardi, M., Schechter, P. L., et al. 2003, *ApJ*, 594, 225
- Shu, Y., Bolton, A. S., Brownstein, J. R., et al. 2015, *ApJ*, 803, 71
- Shu, Y., Bolton, A. S., Mao, S., et al. 2016, *ArXiv e-prints*
- Silk, J. & Rees, M. J. 1998, *A&A*, 331, L1
- Smith, R. J., Lucey, J. R., & Conroy, C. 2015, *MNRAS*, 449, 3441
- Sonnenfeld, A., Gavazzi, R., Suyu, S. H., Treu, T., & Marshall, P. J. 2013a, *ApJ*, 777, 97
- Sonnenfeld, A., Nipoti, C., & Treu, T. 2014, *ApJ*, 786, 89
- Sonnenfeld, A., Treu, T., Gavazzi, R., et al. 2013b, *ApJ*, 777, 98
- Sonnenfeld, A., Treu, T., Marshall, P. J., et al. 2015, *ApJ*, 800, 94
- Sutherland, R. S. & Dopita, M. A. 1993, *ApJS*, 88, 253
- Teyssier, R. 2002, *A&A*, 385, 337
- Tortora, C., La Barbera, F., Napolitano, N. R., et al. 2014, *MNRAS*, 445, 115
- Treu, T., Auger, M. W., Koopmans, L. V. E., et al. 2010, *ApJ*, 709, 1195
- Treu, T., Gavazzi, R., Gorecki, A., et al. 2009, *ApJ*, 690, 670
- Treu, T., Koopmans, L. V., Bolton, A. S., Burles, S., & Moustakas, L. A. 2006, *ApJ*, 640, 662
- Treu, T. & Koopmans, L. V. E. 2002, *ApJ*, 575, 87
- Treu, T. & Koopmans, L. V. E. 2004, *ApJ*, 611, 739
- Tu, H., Gavazzi, R., Limousin, M., et al. 2009, *A&A*, 501, 475
- Tweed, D., Devriendt, J., Blaizot, J., Colombi, S., & Slyz, A. 2009, *A&A*, 506, 647
- van de Voort, F., Schaye, J., Booth, C. M., Haas, M. R., & Dalla Vecchia, C. 2011, *MNRAS*, 414, 2458

- Weinberger, R., Springel, V., Hernquist, L., et al. 2016, ArXiv e-prints
 Welker, C., Dubois, Y., Devriendt, J., et al. 2015, ArXiv e-prints
 White, S. D. M. & Frenk, C. S. 1991, ApJ, 379, 52
 White, S. D. M. & Rees, M. J. 1978, MNRAS, 183, 341
 Wyithe, J. S. B. & Loeb, A. 2003, ApJ, 595, 614
 Xu, D., Springel, V., Sluse, D., et al. 2017, MNRAS, 469, 1824

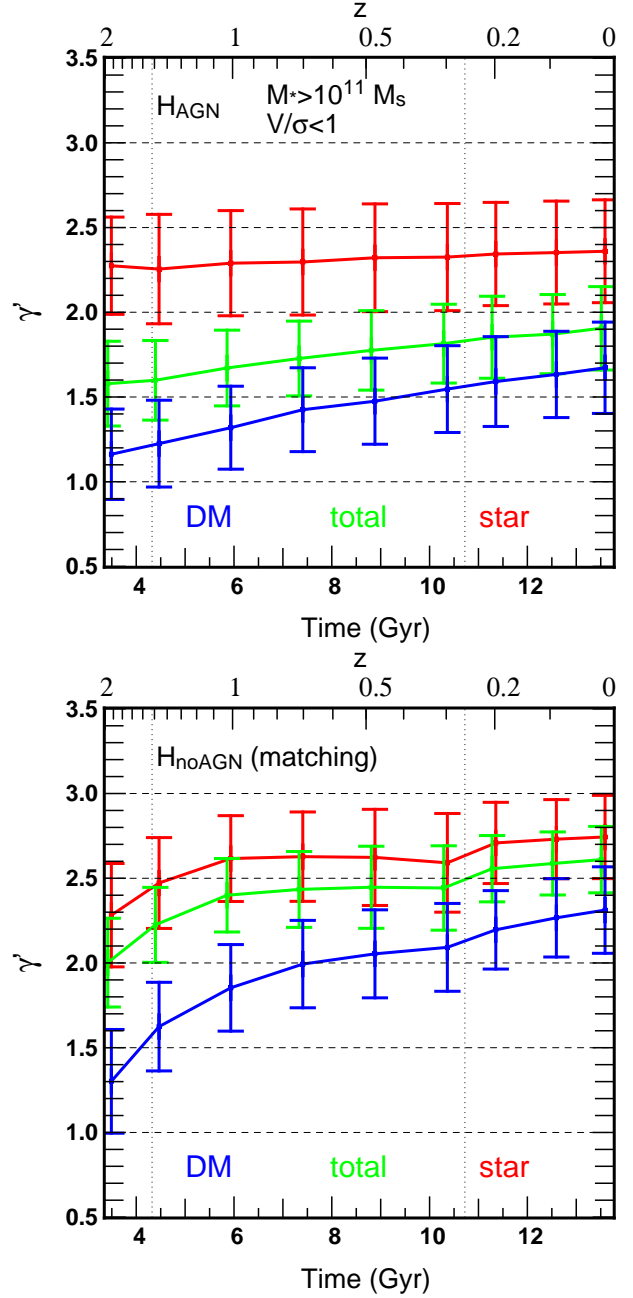


Figure 11. First line: the time evolutions of the mass-weighted total density slope γ'_{tot} (green lines) for H_{AGN} galaxies with $V/\sigma < 1$, a mass greater than $10^{11} M_{\odot}$ [\star and $R_e > 5$ kpc.] We also show the variations of the stellar (γ'_*) and dark matter components (γ'_{dm}) in red and blue lines respectively. The same evolutions derived obtained from the matching H_{noAGN} galaxies are displayed in the second line. Error bars are standard deviations. The dashed lines indicate the times when a new refinement level is added in the simulations.

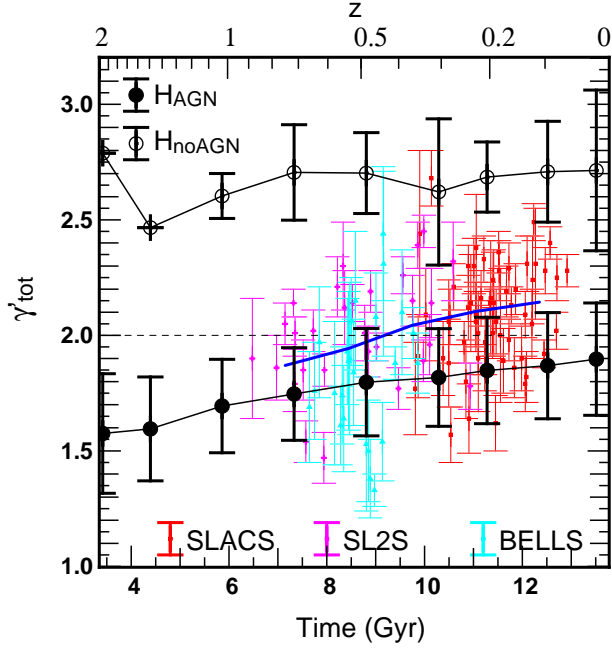


Figure 12. the time evolutions of the mass-weighted total density slope γ'_{tot} (green lines) for H_{AGN} (black points) and H_{noAGN} (white points) galaxies satisfying $V/\sigma < 1$, $M_* \geq 10^{11} M_{\odot}$ and $R_e > 5$ kpc in the considered redshift interval. We also add the observational data from the SLACS (red), SL2S (purple) and BELLS (cyan). [**★ The solid blue line shows the mean evolution of all observational data**]. Error bars are standard deviations.